Interacting tails of asymmetric domain walls: Theory and experiments

Lukas Döring*
RWTH Aachen, Lehrstuhl I für Mathematik, Pontdriesch 14-16, 52056 Aachen, Germany and JARA–Fundamentals of Future Information Technology

Claudia Hengst
IFW Dresden, Institute for Complex Materials, PO 270116, 01171 Dresden, Germany

Felix Otto
Max Planck Institute for Mathematics in the Sciences, Inselstraße 22, 04103 Leipzig, Germany and Universität Leipzig, Mathematisches Institut, PF 100920, 04009 Leipzig, Germany

Rudolf Schäfer
IFW Dresden, Institute for Metallic Materials, PO 270116, 01171 Dresden, Germany and Dresden University of Technology, Institute for Materials Science, PO 01062 Dresden, Germany
(Received 19 February 2015; revised manuscript received 23 July 2015; published 19 January 2016)

In this paper, we address the structure and interaction of neighboring asymmetric Néel and Bloch walls in soft ferromagnetic films. First, we review a recent reduced model for the structure of parallel systems of asymmetric walls with potentially interacting tails and provide a derivation via the method of matched asymptotic expansions, starting from the micromagnetic-torque equation. Then, we report on experimentally observed domain-wall transitions under a varying hard-axis field in $Co_{40}Fe_{40}B_{20}$ films. Upon the wall transition, the average hard-axis magnetization in the domains increases significantly, by an amount that depends on the width of the domains. For films of moderate thickness, the hard-axis magnetization jump that the theory predicts excellently agrees with the experimental data. Hence, we conclude that interacting tails of neighboring asymmetric Néel walls cause the observed additional rotation of the magnetization towards large hard-axis fields.

DOI: 10.1103/PhysRevB.93.024414

I. INTRODUCTION

Even though magnetic domain walls in ferromagnetic films have been under experimental and theoretical investigation for a long time, a general theory that describes their properties and structure is not yet available. Depending on the film thickness, the magnetic properties of the material, and applied magnetic fields, different wall types may be energetically favored. Figure 1 shows a phase diagram that indicates the wall type of least energy in films of permalloy and CoFeB, depending on the normalized film thickness t/d and the reduced field $H = \frac{|\vec{H}|}{H_K}$, for the two material-dependent quality factors $Q = \frac{K_u}{K_d}$. Here, H_K denotes the anisotropy field, K_u the first-order anisotropy constant, $d = \sqrt{A/K_d}$ the Bloch linewidth, A the exchange constant, and $K_d = \frac{1}{2}\mu_0 M_s^2$ the demagnetizing constant of the material with the vacuum permeability μ_0 and the saturation magnetization M_s. In this paper, we will only consider soft materials, i.e., $Q \ll 1$.

In very thin films, symmetric Néel walls are observed with a magnetization profile that splits into a narrow core region with an extension of the order of $\sim d^2/t$ and extended tails with a logarithmically decaying magnetization over a width $w_{\text{tails}} \sim t/Q$. For low-anisotropy materials, the dominant contribution to the energy of symmetric Néel walls is the stray field generated in their tails.

For intermediate film thicknesses, cross-tie walls are observed which consist of a series of Bloch lines and 90° Néel wall segments in between [2–5]. Note that the results presented below do not allow for a prediction of the cross-tie wall energy, which is therefore not present in the phase diagram (see Ref. [5] for a recent numerical treatment of the case of 180° walls).

In thicker films, partially or completely stray-field free domain walls are energetically favored, namely the asymmetric Néel wall and asymmetric Bloch wall [6,7]. In contrast to the asymmetric Bloch wall, the asymmetric Néel wall reduces its energy by splitting off an extended tail. A vortex pattern is formed within the wall core, which avoids most of the dipolar charge. Typically, about 10% of the dipolar charges are distributed in the tails of asymmetric Néel walls. With increasing hard-axis field, the contribution of the tails to the total magnetization rotation increases until—at a critical field value—the asymmetric core disappears in favor of a symmetric Néel wall structure [cf. Ref. [1], Sec. 3.6.4 (E)]. A similar continuous transition from symmetric to asymmetric Néel walls occurs with increasing film thickness [5,8]. For a more detailed review on magnetic domain walls in thin films, we refer the reader to Ref. [1] and references therein.

The existence of different wall types as well as the occurrence of domain wall transitions in an applied field is of practical relevance for various applications. For instance it has been shown recently that the high-frequency magnetization response of domain structures is significantly altered due to a network of interacting neighboring walls [9]. As the acoustic domain resonance frequency depends on the effective

*L.Doering@math1.rwth-aachen.de

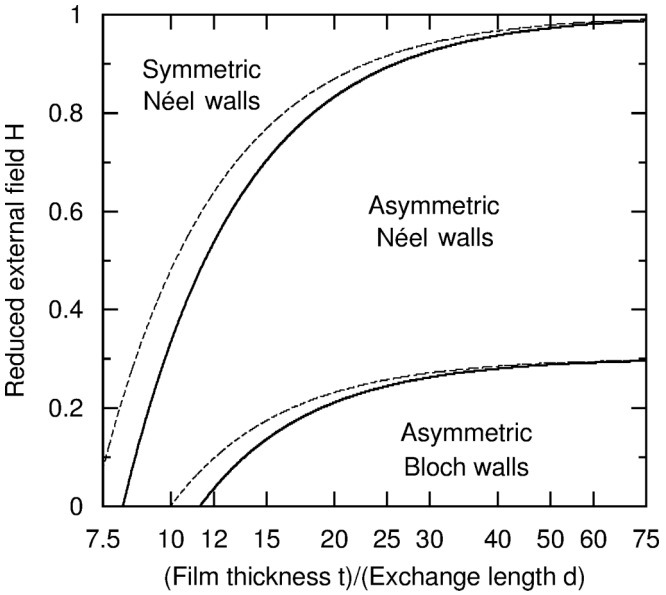

FIG. 1. Phase diagram according to (5) for nanocrystalline permalloy and amorphous CoFeB, i.e. $Q = 2.5 \times 10^{-4}$ (solid lines) and $Q = 1.55 \times 10^{-3}$, respectively. Note that compared to Ref. [1], Fig. 3.80, the transition between symmetric and asymmetric Néel walls is shifted towards larger fields.

domain wall width and on the interaction strength between neighboring domain walls, either smooth or step-like changes (of the order of 0.5 GHz) of the domain resonance frequency can be observed due to domain wall transformations. For the quantification of such effects, the knowledge of the internal structure of a domain wall, i.e., its width and the strength of interaction with walls in the neighborhood is indispensable.

The interaction between neighboring symmetric Néel walls by an overlap of their extended tails has been demonstrated to significantly determine the energy balance and structure of the domain walls [1]. Whereas wall interaction does not play a dominant role for stray-field free asymmetric Bloch walls, it can still be significant for the energy and magnetization configuration of neighboring asymmetric Néel walls [10].

The analysis of domain walls very much depends on the specific wall type: On one hand, the one-dimensional nature of symmetric Néel walls makes both their numerical [11] and analytic [12–15] treatment possible. On the other hand, the structure of asymmetric Bloch walls is only accessible to Ritz methods [6,7] or numerical micromagnetics [5,16,17], which is feasible due to the small wall width. For asymmetric Néel walls, the combination of a two-dimensional wall pattern with long-range extended tails makes this type of wall difficult to study by numerical simulation [1,5,17].

The numerical results in Ref. [18] show that the transition between the asymmetric wall types is hysteretic (see also Ref. [19]). However, the interaction of extended wall tails seems to influence the domain magnetization more strongly than expected (see Fig. 7).

Recently, a step towards a quantitative understanding of the splitting of asymmetric Néel walls into stray-field free core and logarithmic tails has been undertaken. In Ref. [20] an asymptotic limit of the micromagnetic energy functional was derived that yields a precise description of the relative

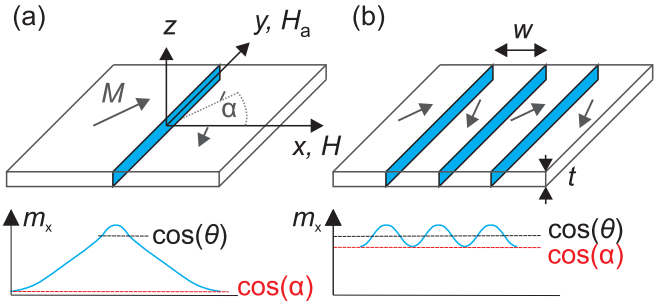

FIG. 2. Domain configuration (top) considered in the reduced model for (a) an isolated domain wall (blue) and (b) a system of domain walls at distance w in an extended film of thickness t. The bottom row *schematically* illustrates the magnetization component m_x on the film surface with core ($m_x > \cos\theta$) and tail region ($m_x > \cos\alpha$) of asymmetric walls.

amount of rotation in stray-field free wall core and logarithmic wall tails for an isolated domain wall. The results have been generalized to systems of interacting domain walls [21].

Here, we briefly summarize the main results of Refs. [20,21] and compare the theoretical with experimental results for $Co_{40}Fe_{40}B_{20}$ films. Thereby we aim to demonstrate the validity of the proposed model, which can be easily applied for various magnetic thin film materials. Additionally, we provide an alternative derivation of the reduced models that focuses on the torque balance between magnetic moments and effective field instead of energy considerations.

II. THEORY

Consider a ferromagnetic film with uniaxial anisotropy ($||y$), a thickness t with $-\frac{t}{2} \leqslant z \leqslant \frac{t}{2}$, and infinite extensions in the film plane (xy plane). For the presence of magnetic domain walls in the film two cases will be distinguished, as sketched in Fig. 2.

In a first case (a) we assume that two domains of constant magnetization $\vec{m}(x = \pm\infty) = (\cos\alpha, \pm\sin\alpha, 0)$ have formed and are separated by a domain wall. Then, in a second case (b) a system of domain walls is considered that are equally spaced at a distance w and which may interact via extended wall tails. The energy of isolated and interacting domain walls in an external field $\vec{H}_{\rm ext}||x$ is derived starting from the Landau-Lifshitz energy (see, e.g., Ref. [1], Sec. 3.2):

$$\mathbb{E} = A \int |\operatorname{grad} \vec{m}|^2 dV - \frac{1}{2}\mu_0 M_s \int \vec{H}_d \cdot \vec{m}\, dV + K_u \int (1 - (\vec{m}\cdot\vec{e})^2) dV - \mu_0 M_s \int \vec{H}_{\rm ext} \cdot \vec{m}\, dV, \quad (1)$$

with the magnetization vector $\vec{m} = \frac{\vec{M}}{M_s}$, the stray or demagnetizing field $\vec{H}_d$, and $\vec{e}\,||y$ the anisotropy axis. By dV we denote the volume element.

To make the problem accessible to a mathematical treatment, we assume that all domain walls are parallel to the y axis and the magnetization configuration is translation invariant in y, so that it suffices to study the energy density per length in the y direction. Note, however, that this assumption excludes

the formation of Bloch lines and wall segmentation as it occurs for cross-tie walls.

A. A reduced model for domain walls in moderately thin films

In order to reduce the number of physical parameters in the problem, we employ the K_d-based nondimensionalization [22] of Eq. (1). On a cross section of the sample in the xz plane with area element dA, we obtain:

$$E = d^2 \int |\operatorname{grad} \vec{m}|^2 dA + \int_{\mathbb{R}^2} |\vec{h}_d|^2 dA + Q \int \left((m_x - H)^2 + m_z^2\right) dA, \tag{2}$$

with $\vec{H}_d = M_s \vec{h}_d$ and $\vec{H}_{\text{ext}} = H_K(H,0,0) = M_s Q(H,0,0)$. The quantity H denotes the reduced external field. Note that while passing from Eqs. (1) to (2), we have also added the normalizing constant $Q \int H^2 dA$ to ensure that each of the constant magnetization configurations $\vec{m} = (H, \pm\sqrt{1-H^2}, 0)$ has vanishing energy density. Moreover, E is only partially nondimensional and has units of area.

In the regime $Q \ll (\frac{t}{d})^2 \ll Q^{-1}$ and for a wall angle $2\alpha = 180^\circ$, the minimal wall energy (2) per unit domain wall length is known [23] to scale as follows (up to a multiplicative constant):

$$E_{\text{wall}} \sim \begin{cases} t^2 \ln^{-1} \frac{1}{Q}, & \text{if } \left(\frac{t}{d}\right)^2 \leqslant \ln \frac{1}{Q}, \\ d^2, & \text{if } \left(\frac{t}{d}\right)^2 \geqslant \ln \frac{1}{Q}. \end{cases}$$

In thin films, the minimal-energy scaling $E_{\text{wall}} \sim \frac{\pi}{2} t^2 \ln^{-1} \frac{1}{Q}$ is satisfied by symmetric Néel walls (see also Refs. [22], Sec. 4.6.2, and [13]). In thicker films, the minimal-energy scaling $E_{\text{wall}} \sim d^2$ is satisfied by, e.g., a stray-field free asymmetric Bloch wall.

Thus, in order to analyze both symmetric and asymmetric walls, in particular asymmetric Néel walls with extended tails, it seems most promising to focus on the critical regime of the crossover from symmetric to asymmetric wall types, i.e., the asymptotic regime $(\frac{t}{d})^2 \sim \ln \frac{1}{Q}$ as $Q \downarrow 0$. In this regime, for sufficiently large (reduced) hard-axis field $H \in [0,1]$, one expects to recover a domain wall of Néel instead of Bloch type. In Refs. [20,21], it has been shown mathematically rigorously that in this regime and both for isolated and interacting walls the internal structure of an arbitrary domain wall can be determined by analyzing a simple scalar minimization problem.

We will describe the result for the periodic case (b): One may assume that the width $w \gg t$ of the domains is strictly smaller than the width t/Q of the tails of symmetric Néel walls that are constrained only by anisotropy. Otherwise, one does not expect interaction of the walls and may treat each domain wall independently. In particular, for $w \ll t/Q$ it is expected that the wall tails invade the whole domain. Thus, to leading order in $w/t \uparrow \infty$, the sum of stray-field and anisotropy/Zeeman energy of logarithmic wall tails that connect the magnetization $m_x = \cos\theta$ in the core to $m_x = \cos\alpha$ in the center of a domain (cf. Fig. 2) is given by

$$E_{\text{tails}}(\theta,\alpha,H) := \frac{\pi}{2} t^2 \frac{(\cos\theta - \cos\alpha)^2}{\ln \frac{w}{t}} + Qwt(\cos\alpha - H)^2.$$

Optimizing the angle α, we find that the magnetization in the center of the domain is given by

$$\cos\alpha_{\text{opt}} = H + \frac{\pi t}{\pi t + 2Qw \ln \frac{w}{t}} (\cos\theta - H). \tag{3}$$

In particular, one identifies the interesting regime of periods

$$w \sim \frac{t}{Q \ln(1/Q)},$$

in which a nontrivial $\cos\alpha_{\text{opt}} \notin \{\cos\theta, H\}$ is possible [24]. Surprisingly, the domain width w needs to be by $\ln(1/Q)$ smaller than the guess t/Q (coming from the width of the anisotropy-constrained Néel wall tails) for the critical regime of periods.

The optimal angle θ for the transition from stray-field free wall core to the logarithmic tails under the reduced external field H can be found by optimizing the sum of the minimal exchange energy $E_{\text{core}}(\theta)$ of a stray-field free wall core [25] of wall angle θ and the energy of the optimal wall tails:

$$E_{\text{wall}}(H) \approx \min_\theta \Big(E_{\text{core}}(\theta) + \underbrace{\min_\alpha E_{\text{tails}}(\theta,\alpha,H)}_{= \frac{\pi}{2} t^2 \frac{2Qw}{\pi t + 2Qw \ln \frac{w}{t}} (\cos\theta - H)^2} \Big). \tag{4}$$

Choosing [26] $w \gg t/(Q \ln \frac{1}{Q})$, one recovers for $Q \ll 1$ a reduced model for the structure of an isolated domain wall (a):

$$E_{\text{wall}}(H) \approx \min_\theta \left(E_{\text{core}}(\theta) + \frac{\pi}{2} \frac{t^2}{\ln \frac{1}{Q}} (\cos\theta - H)^2 \right). \tag{5}$$

On the other hand, for $w \ll t/(Q \ln \frac{1}{Q})$, the tail contribution to Eq. (4) becomes negligible, and one finds $\theta_{\text{opt}} \approx \alpha_{\text{opt}} \approx 0$.

The structure of Eqs. (4) and (5) confirms and quantifies the description of asymmetric Néel walls as an optimal combination of stray-field free wall cores with extended tails given in Ref. [1], Sec. 3.6.4 (E). In other words, the above results demonstrate that asymmetric Néel walls have two internal parameters—the core and domain wall angles θ and α—that the wall optimizes automatically to produce the lowest micromagnetic energy given a reduced external field H.

Note that this explanation (and also the rigorous proof in Refs. [20,21]) takes an *energetic* point of view and is precise only in the limit $Q \downarrow 0$. In the following section, we will demonstrate that asymptotically the same result (4) can be derived starting from the micromagnetic equations in the form of a *torque balance*, using the method of matched asymptotic expansions. Moreover, this approach potentially yields slightly more precise quantitative results for positive $0 < Q \ll 1$.

B. Matching core and tails by asymptotic expansions

We will focus on the periodic case (b): The starting point in the method of matched asymptotic expansions is the first variation of the micromagnetic energy in its nondimensionalized form (2)

$$\vec{m} \times \left(-d^2 \triangle \vec{m} - \vec{h}_d + Q \begin{pmatrix} m_x - H \\ 0 \\ m_z \end{pmatrix} \right) = 0 \quad \text{for} \quad |z| < \frac{t}{2},$$
$$\partial_z \vec{m} = 0 \quad \text{for} \quad |z| = \frac{t}{2}. \tag{6}$$

This torque balance has to be supplemented by (quasistatic remnants of) Maxwell's equations, expressed in terms of the stray-field potential u (that is, $h_d = -\operatorname{grad} u$):

$$\begin{aligned} \triangle u &= \operatorname{div} \vec{m} \quad \text{for} \quad |z| < \frac{t}{2}, \\ [-\partial_z u] &= m_z \quad \text{for} \quad z = \pm\frac{t}{2}, \\ \triangle u &= 0 \quad \text{for} \quad |z| > \frac{t}{2}. \end{aligned} \tag{7}$$

We will assume that the configuration has the symmetry of the asymmetric Néel wall, i.e., that it is invariant under the transformation $(x,z) \to -(x,z), m_y \to -m_y, u \to -u$ at each wall core.

We first turn to the core or *inner* region in the parlance of matched asymptotics. Because this region is small, it can afford a z-dependent magnetization pattern that to leading order avoids magnetic charges. Likewise, the effects of anisotropy and external field are negligible. Hence in this region, Eqs. (6) and (7) are well approximated by

$$\left.\begin{aligned} \vec{m}_{\text{in}} \times \left(-\triangle \vec{m}_{\text{in}} + \operatorname{grad} \tfrac{u_{\text{in}}}{d^2}\right) = 0 \\ \operatorname{div} \vec{m}_{\text{in}} = 0 \end{aligned}\right\} \quad \text{for } |z| < \frac{t}{2}, \\ \partial_z (m_{\text{in},x}, m_{\text{in},y}) = 0 \text{ and } m_{\text{in},z} = 0 \quad \text{for } |z| = \frac{t}{2}. \tag{8}$$

In the first equation, the (reduced) stray-field potential $\frac{u_{\text{in}}}{d^2}$ plays the role of a Lagrange multiplier for the divergence-free condition in the second equation, like the pressure in the equations describing an incompressible fluid. We learn from Eq. (8) that the only length scale for the core is the film thickness t. For all physically relevant solutions of Eq. (8), the asymptotic behavior (i.e., for large $|x|$) of the magnetization $\vec{m}_{\text{in}}$ is of the form

$$\vec{m}_{\text{in}} \approx (\cos\theta, \pm\sin\theta, 0) \quad \text{for } \pm x \gg t \tag{9}$$

for *some* angle θ, which we interpret as the amount of magnetization rotation in the asymmetric core. In fact, there are two and only two continuous branches $\theta \mapsto \vec{m}_{\text{in},\theta}$ of solutions of Eq. (8) with Eq. (9) that correspond to the core of an asymmetric Néel (as opposed to Bloch) wall. Both are related by a reflection $z \to -z, m_z \to -m_z$ and hence have the same energy. They intersect only for the angle $\theta = 0$, where $\vec{m}_{\text{in},\theta} = (1,0,0)$. Under smooth changes of the external field H, the relevant solutions will be on the same branch, which effectively makes the relevant $\vec{m}_{\text{in},\theta}$ uniquely defined. In line with the discussion that leads to the approximation (8), the energy of $\vec{m}_{\text{in},\theta}$ is given by

$$E_{\text{core}}(\theta) = d^2 \int |\operatorname{grad} \vec{m}_{\text{in},\theta}|^2 dA. \tag{10}$$

This now allows us to characterize the asymptotic behavior also of the stray-field potential u:

$$4t(\sin\theta) u_{\text{in}} \approx \pm \frac{dE_{\text{core}}}{d\theta} \quad \text{for } \pm x \gg t. \tag{11}$$

We note that Eq. (11) follows from using Eq. (9) after integrating in x the identity

$$\begin{aligned} &\frac{d}{d\theta}\frac{1}{2}\int_{-\frac{t}{2}}^{\frac{t}{2}} |\operatorname{grad} \vec{m}_{\text{in},\theta}|^2 dz \\ &\quad = \frac{d}{dx}\int_{-\frac{t}{2}}^{\frac{t}{2}} \left(\partial_x \vec{m}_{\text{in},\theta} \cdot \partial_\theta \vec{m}_{\text{in},\theta} - \frac{u_{\text{in}}}{d^2}\partial_\theta m_{\text{in},\theta,x}\right) dz, \end{aligned}$$

which belongs to the realm of equipartition of energy statements and easily follows from multiplying Eq. (8) with $\partial_\theta \vec{m}_{\text{in},\theta}$.

In the large tail region, the *outer* region, we neglect variations of the magnetization in the z direction, neglect the m_z component, and project all the magnetic charges into the $\{z = 0\}$ plane, so that Eq. (7) turns into

$$\begin{aligned} \partial_z u_{\text{out}}(z = 0^+) - \partial_z u_{\text{out}}(z = 0^-) \\ = \underbrace{t\partial_x (m_{\text{out},x} - H)}_{= t\partial_x m_{\text{out},x}} \quad \text{for} \quad z = 0, \\ \triangle u_{\text{out}} = 0 \quad \text{for} \quad z \neq 0, \end{aligned} \tag{12}$$

where we denote by $z = 0^+$ and $z = 0^-$ the limits $z \to 0$ with $z > 0$ and $z < 0$, respectively, i.e., the limits from above and below.

On the other hand, in the in-plane projection of the torque balance $\vec{m}|| - d^2\triangle\vec{m} - \vec{h}_d + Q((m_x - H)\vec{e}_x + m_z\vec{e}_z)$, cf. Eq. (6), we neglect the exchange term and arrive at $(m_x, m_y)||(\partial_x u + Q(m_x - H), \partial_y u = 0)$, which, as long as $m_y \neq 0$, i.e., away from the wall cores, implies [27]

$$\partial_x u_{\text{out}} + Q(m_{\text{out},x} - H) = 0 \quad \text{for} \quad z = 0,\ x \notin w\mathbb{Z}. \tag{13}$$

We note that Eqs. (12) and (13) form a system of *linear* equations for $(u_{\text{out}}, m_{\text{out},x} - H)$, with a one-dimensional set of physically relevant solutions. The two relevant length scales are w and t/Q. It is also convenient to choose the multiplicative degree of freedom A_{out} such that it normalizes the near-field behavior

$$u_{\text{out}} = \pm A_{\text{out}} \quad \text{for } z = 0 \text{ and } x = 0^{\pm}, \tag{14}$$

periodically extended.

Equating the inner and outer approximation to the stray-field potential, that is, u_{in} from Eq. (11) and u_{out} from Eq. (14), in the intermediate region $t \ll x \ll w$ yields the first matching condition

$$A_{\text{out}} = \frac{1}{4t\sin\theta}\frac{dE_{\text{core}}}{d\theta}. \tag{15}$$

The second matching condition comes from equating the magnetizations: The Fourier transform of the solutions of Eqs. (12) and (13) can be determined explicitly. For fixed $m_{\text{out},x}$, equation (12) is solved by

$$\begin{aligned} \mathcal{F}(u_{\text{out}})(k,z) = -t\frac{\mathcal{F}(\partial_x(m_{\text{out},x} - H))(k,z)}{2|k|} e^{-|k||z|}, \\ k \in \frac{2\pi}{w}\mathbb{Z}. \end{aligned}$$

Multiplying (13) by e^{-ikx}, integrating the result in x on $[0,w)$ and using the above, one finds

$$\mathcal{F}(m_{\text{out},x} - H)(k) = \frac{2A_{\text{out}}}{Q + \frac{t}{2}|k|}, \quad k \in \frac{2\pi}{w}\mathbb{Z}. \tag{16}$$

The value $2A_{\text{out}} = u_{\text{out}}(x = 0^+) - u_{\text{out}}(x = w^-)$ for $z = 0$ enters due to an integration by parts in x that removes the derivative on u_{out}.

From Eq. (16) one can now read off the profile of the wall tails:

$$m_{\text{out},x} - H = \frac{2A_{\text{out}}}{w} \sum_{k \in \frac{2\pi}{w}\mathbb{Z}} \frac{\cos(xk)}{Q + \frac{t}{2}|k|} = \frac{2A_{\text{out}}}{Qw} \sum_{n \in \mathbb{Z}} \frac{\cos\left(2\pi \frac{x}{w} n\right)}{1 + \frac{\pi t}{Qw}|n|}.$$

Using $Qw/t \ll 1$, we compute

$$\begin{aligned} & m_{\text{out},x} - H \\ &= \frac{2A_{\text{out}}}{Qw}\left(1 + \frac{2Qw}{\pi t} \sum_{n=1}^{\infty} \frac{\cos\left(2\pi \frac{x}{w} n\right)}{\frac{Qw}{\pi t} + n}\right) \\ &= \frac{2A_{\text{out}}}{Qw}\left(1 + \mathcal{O}\left(\frac{2Qw}{\pi t}\right) + \frac{2Qw}{\pi t} \underbrace{\sum_{n=1}^{\infty} \frac{\cos\left(2\pi \frac{x}{w} n\right)}{n}}_{=\mathcal{O}(1)+\ln(w/x)}\right) \\ &\approx \frac{2A_{\text{out}}}{Qw}\left(1 + \frac{2Qw}{\pi t} \ln \frac{w}{t}\right), \quad \text{provided } x \sim t. \end{aligned}$$

Equating the inner approximation of the magnetization $m_{\text{in},x}$ in Eq. (9) with the outer approximation $m_{\text{out},x}$ from above in the overlapping range, we obtain

$$\cos\theta - H \approx \frac{2A_{\text{out}}}{Qw}\left(1 + 2\frac{Qw}{\pi t} \ln \frac{w}{t}\right).$$

The two matching conditions (15) and the above combine to

$$\frac{dE_{\text{core}}}{d\theta} + \pi t^2 \frac{2Q\frac{w}{t}}{\pi + 2Q\frac{w}{t}\ln\frac{w}{t}}(\cos\theta - H)(-\sin\theta) = 0.$$

This equation is precisely the first variation of Eq. (4) in θ.

Additionally, one computes the domain average of m_x in the periodic case by evaluating the zeroth Fourier mode $\mathcal{F}(m_{\text{out},x} - H)(k = 0) = 2A_{\text{out}}/Q$ using the second matching condition:

$$\frac{1}{w}\int_0^w m_{\text{out},x}\, dx = H + \frac{2A_{\text{out}}}{Qw} = H + \frac{\pi}{\pi + 2Q\frac{w}{t}\ln\frac{w}{t}}(\cos\theta - H).$$

Another way of deriving this reduced model consists in studying isolated walls, which decay quadratically for $|x| \gg t/Q$, by similar methods. The superposition of wall tails coming from walls at centers $x \in w\mathbb{Z}$ can be shown to yield the same result as the above Fourier approach.

C. Evaluation of the theoretical results for different material parameters

In the following, we aim to apply the reduced model for interacting tails of asymmetric domain walls using realistic thin film parameters and derive (i) hard axis magnetization curves depending on the domain wall spacing w, (ii) magnetization changes resulting from the Bloch-Néel wall transition under applied magnetic fields, and (iii) the contribution of the wall core to the overall magnetization rotation in the walls. We employ the material parameters shown in Table I which correspond to the samples that will be studied in Sec. III.

TABLE I. Sample properties of extended reference films.

Sample No.	Film thickness (nm)	$\mu_0 H_a$ (mT)	Q ($\times 10^{-3}$)
1	102	2.02	1.36
2	153	1.37	0.93
3	212	1.72	1.16

Figure 3 displays the hard-axis magnetization $m_x(w/2)$ that is obtained by minimizing Eq. (4) in θ for the material parameters of sample 1 (cf. Table I). The value $m_x(w/2) \approx \cos\alpha_{\text{opt}}$ is obtained from the optimal $\theta = \theta_{\text{opt}}$ in Eq. (4) by evaluating Eq. (3). As the energy of the asymmetric wall core, we use the exchange energy of numerically determined exactly stray-field free asymmetric Bloch and Néel walls, cf. Eq. (10). As expected, the choice of material parameters and the tail energy contribution is irrelevant along the Bloch wall branch $m_x(w/2) \approx H$.

As expected, Fig. 3 shows that neighboring walls interact more strongly, i.e., entail stronger hysteresis, the narrower the domains are. Note that in the experimentally relevant range of reduced fields $H \in [0,0.35]$, $m_x(w/2)$ is almost linear in H. Since the instability fields of Néel and Bloch wall seem unavailable within the reduced model [28], we will therefore use the value $m_x(w/2)$ for zero field $H = 0$ and Néel wall cores to predict the jump $\Delta m_x(w/2)$ between Néel and Bloch magnetization branches at instability.

Figure 4 predicts a strong interaction of neighboring wall tails as soon as the domain period w falls below $\sim 0.2t/Q$. This

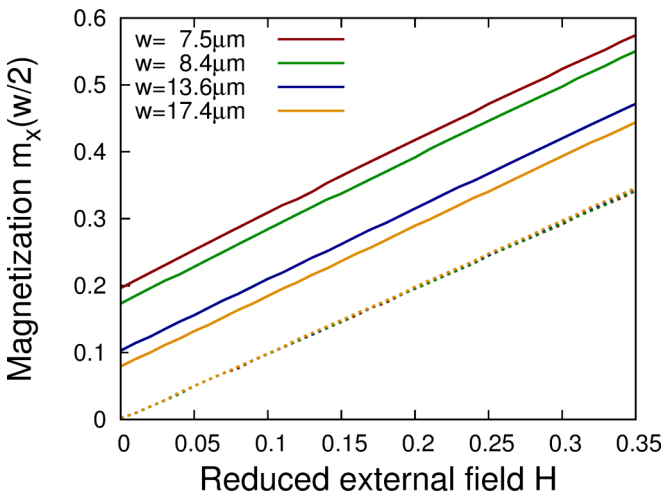

FIG. 3. Predicted hard-axis magnetization curves for the reduced model (4) with asymmetric Néel cores. The prediction for asymmetric Bloch walls (dotted lines) is essentially independent of domain widths, sample dimensions, and material parameters. Material parameters are those of sample 1.

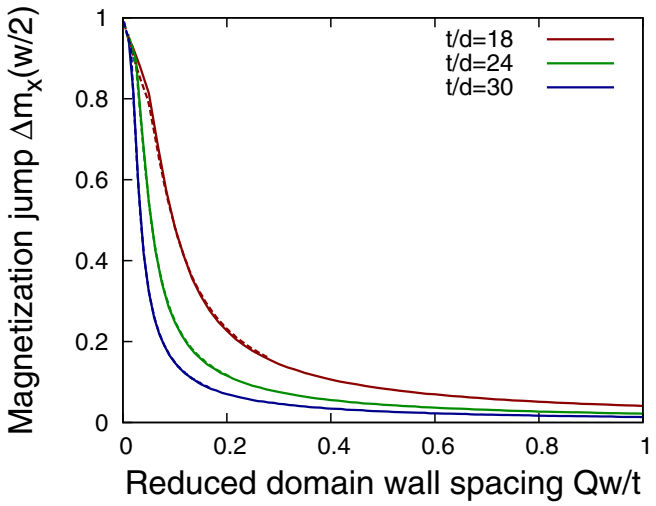

FIG. 4. The hard-axis magnetization (3) at zero field $H = 0$ for Néel wall cores serves as a prediction for the magnetization jump between the almost linear Bloch and Néel wall branches. The curves for amorphous CoFeB (solid lines, $Q = 1.5 \times 10^{-3}$) and nanocrystalline permalloy (dashed lines, $Q = 2.5 \times 10^{-4}$) are virtually indistinguishable.

threshold decreases with increasing reduced film thickness t/d.

Finally, Fig. 5 shows the relative amount of rotation $\theta_{\text{opt}}/\alpha$ in wall core and tails for the parameters from samples 1 and 2 in percent as a function of the reduced external field. One observes that for small reduced external field $H \approx 0.3$, in both samples and independent of the domain width, about 90–95% of the rotation falls upon the core. At larger fields, the tails gain importance until at fields $H_{AS} \approx 0.75$–0.9, depending on the film thickness and domain width, the asymmetric wall core vanishes. The critical field H_{AS} increases with the normalized film thickness t/d, domain width w/t, and inverse anisotropy

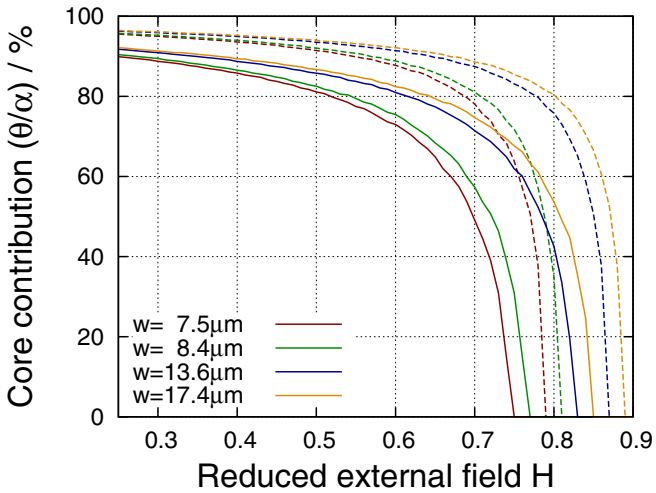

FIG. 5. A prediction according to (4) of the relative amount of rotation in the asymmetric wall cores for the samples 1 (solid lines) and 2 (dashed lines) for various domain wall spacings, cf. Table I.

quality factor $1/Q$. It can be shown to have the value

$$H_{AS} \approx 1 - 4\frac{\pi + 2Q\frac{w}{t}\ln\frac{w}{t}}{\left(\frac{t}{d}\right)^2 Q\frac{w}{t}},$$

provided this number is non-negative. Note that formally, for $w = t/Q$, $Q \ll 1$, we obtain

$$H_{AS} \approx 1 - 8\left(\frac{d}{t}\right)^2 \ln\frac{1}{Q}$$

as critical field for the transition from asymmetric to symmetric Néel wall in an infinitely extended soft ferromagnetic film without interaction of neighboring wall tails.

III. EXPERIMENTS

In this section, we are going to address the transition between the asymmetric wall types in a varying hard-axis field from an experimental point of view. In particular, we will compare the predicted hard-axis magnetization $m_x(w/2)$ in the domain center (cf. Fig. 3) and the magnetization jump $\Delta m_x(w/2)$ (cf. Fig. 4) to the corresponding experimental data (cf. Figs. 7 and 9). In fact, the *experimental* observation of strongly hysteretic wall transitions in the presence of nearby walls has originally motivated the *theoretical* study of interacting walls.

Instead of permalloy, the most popular material used for soft magnetic film studies, we have chosen amorphous CoFeB films for the experimental part. Compared to permalloy with a typical nanocrystalline microstructure, they have similar magnetic properties but are lacking significant ripple modulations of magnetization within the domains. The absence of such disturbing inhomogeneity is favorable for subtle domain wall studies.

A. Sample preparation

Ferromagnetic films of amorphous $Co_{40}Fe_{40}B_{20}$ of varying thicknesses were prepared on glass wafers by means of ultrahigh-vacuum magnetron sputtering at room temperature [29]. An in-plane magnetic field of $\mu_0 H_{\text{dep}} = 25$ mT was applied during film deposition to induce a uniaxial magnetic anisotropy. When studying the interaction between adjacent magnetic domain walls, one should ideally consider different magnetic domain configurations in *extended* films as the effects of domain wall pinning at domain wall triple junctions, and structural edges are reduced [1]. However, lateral patterning was found to be required to allow for the creation of well defined magnetic domains with antiparallel magnetization and a narrow distribution of magnetic domain wall spacings. Therefore, arrays of stripe-shaped structures with in-plane dimensions of 60 μm × 9500 μm and the long axis perpendicular to the induced anisotropy axis were patterned using photolithography. A stripe width of 60 μm was found to be a good compromise between sufficiently small domain wall spacings and large edge-to-edge separation. The lateral spacing between individual stripes was chosen to be 90 μm to minimize effects originating from interelement magnetostatic interaction. A saturation magnetization of $\mu_0 M_s = 1.48$ T was extracted from out-of-plane magnetization curve measurements of an unpatterned reference film (not shown). Table I summarizes

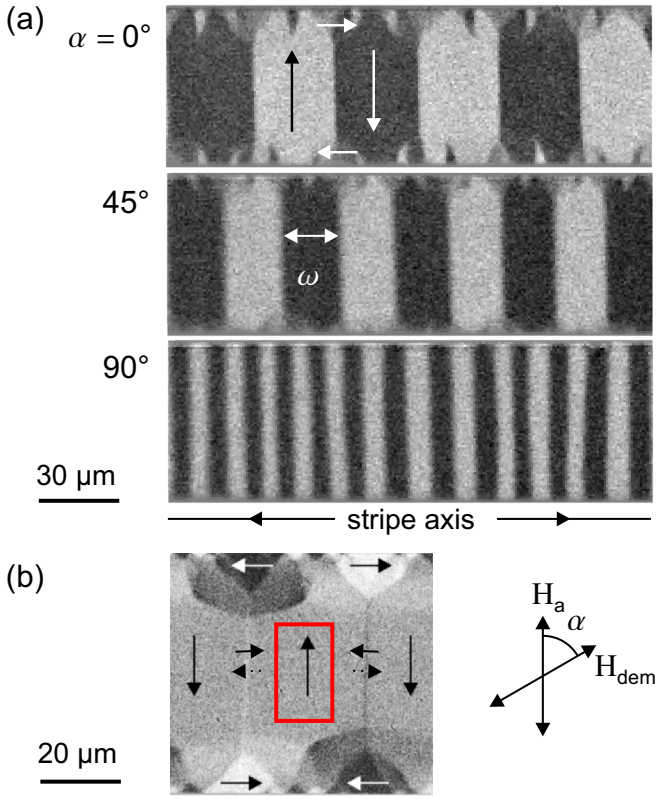

FIG. 6. (a) Kerr images of a stripe section with a thickness of 153 nm after demagnetization with $\vec{H}_{\rm dem}$ under $\alpha = 0°$, 45°, and 90°; arrows indicate the magnetization direction within the domains. (b) The closure domain state studied with transversal Kerr sensitivity shows that the surface magnetization of neighboring 180° domain walls appears equally dark and bright. Dotted arrows indicate the domain wall magnetization at the bottom surface of the film. In order to extract local magnetization curves, only the area highlighted by the red frame was considered.

the different samples, including the film thickness and uniaxial anisotropy field $H_a = |\vec{H}_a|$ as derived from in-plane magneto-optical hysteresis measurements along the magnetic hard axis of reference films (not shown). Slight variations of anisotropy strength may be due to slightly different deposition conditions.

B. Magnetooptical Kerr magnetometry

Flux-closed domain patterns were initialized by demagnetizing the samples in an alternating external magnetic field $\vec{H}_{\rm dem}$ of decreasing amplitude at a frequency of 50 Hz. By varying the in-plane angle α of $\vec{H}_{\rm dem}$ with respect to the anisotropy axis, the magnetic domain wall spacing w was systematically altered from broad domain states (for small α) to narrow domain states with small domain wall spacings (for $\alpha \to 90°$), see exemplarily Fig. 6(a). The domain states, studied by longitudinal magneto-optical Kerr microscopy [1], comprise basic domains with alternating magnetization direction parallel to the induced magnetic easy axis and a closure structure that consists of easy-axis spike domains and closure domains with $\vec{M}$ parallel to the stripe edges. The vertical bright and dark lines in the domain image with

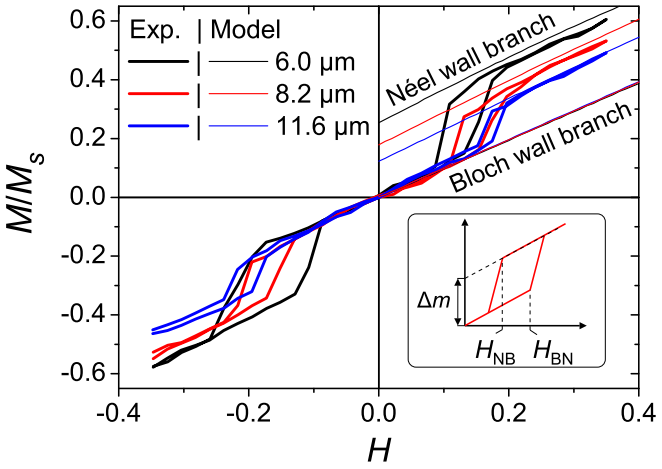

FIG. 7. Minor magnetization loops for three different basic domain widths measured (thick solid lines) in fields perpendicular to the easy axis of magnetization in a sample of 102 nm thickness. In comparison the calculated hysteresis branches (thin solid lines) for cases of asymmetric Néel walls and asymmetric Bloch walls are shown. The inset schematically illustrates the quantification of the magnetization changes that go along with a wall transformation at transition fields $H_{\rm BN}$ and $H_{\rm NB}$.

transverse Kerr sensitivity [Fig. 6(b)] represent the surface magnetization of the 180°-domain walls. From literature [1,30] and due to the fact that the walls appear equally black and white in the images, one can conclude for zero applied field and for the chosen film parameters that these domain walls are asymmetric Bloch walls. A slight mismatch between the induced easy axis of magnetization and the short axis of the elements was introduced during patterning. However, this should not effect the magnetization behavior in hard axis fields in a field range, where closure domains are still present.

Subsequently, a static magnetic field $\vec{H}$ was applied perpendicular to the 180° domain walls, i.e., parallel to the hard axis of magnetization. The domain structure adapts to the increasing hard axis field by rotational magnetization processes inside the basic domains and by growth of the preferentially magnetized ($\vec{M}$ along $\vec{H}$) closure domains. The evolution of the Kerr intensity parallel to the applied field was recorded for the center area of the basic domains [compare red frame in Fig. 6(b)]. The local magnetization curves of several domains with similar domain wall spacing were averaged and normalized with respect to the Kerr intensity at saturation. As during this hysteresis measurement the maximum applied field amplitude was always smaller than the saturation field of the stripes, any irreversible effects originating from domain nucleation have been reduced. This procedure allows for the local recording of minor domain magnetization curves depending only on the domain wall spacing and the film thickness. Minor domain magnetization loops are demonstrated in Fig. 7 for different domain wall spacings w and a film thickness of 102 nm.

For sufficiently small domain wall spacings a jump in the transverse domain magnetization is observed at fields $H_{\rm BN}$ and $H_{\rm NB}$ for increasing and decreasing field, respectively, with $|H_{\rm BN}| > |H_{\rm NB}|$ (see inset in Fig. 7). With decreasing domain wall spacing this hysteresis gets broader and the corresponding

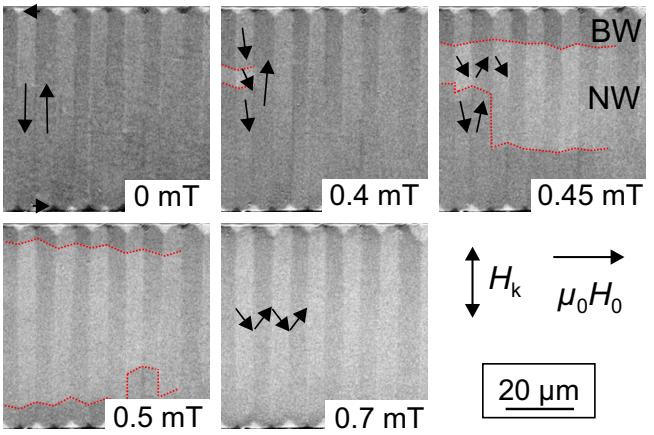

FIG. 8. Kerr images of a $Co_{40}Fe_{40}B_{20}$ stripe section (thickness: 102 nm). The left image in the first row corresponds to the demagnetized state with $\vec{H}_{dem}$ applied at an angle of $\alpha = 90°$ with respect to $\vec{H}_k$. Subsequently a transversal field of increasing amplitude is applied as indicated in the domain images. At $\mu_0 H_0 = 0.4$ mT a superdomain structure emerges, which is highlighted by a dotted line for better visibility. The superdomain expands towards the stripe edges as the transversal field amplitude increases. The formation of a superdomain structure is provoked by the transition of the center wall segments from asymmetric Bloch wall (BW) to asymmetric Néel wall (NW).

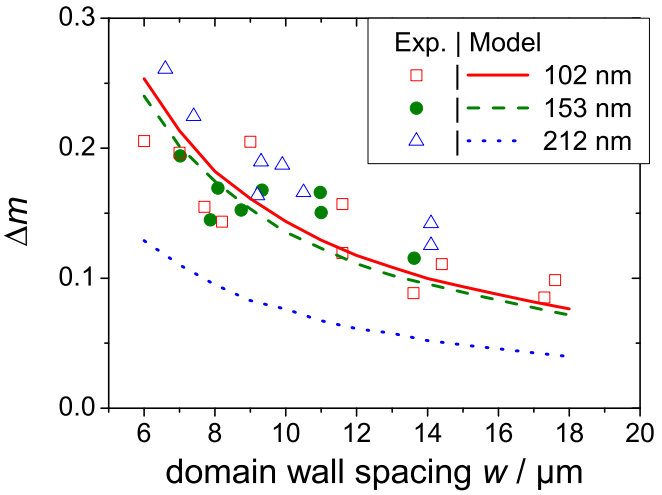

FIG. 9. Change of the transversal magnetization due to the transition between asymmetric Bloch and asymmetric Néel walls under the action of an applied transversal field. The theoretical values are calculated using the reduced model (4) with experimentally determined material parameters and an exchange constant of $A = 1.3 \times 10^{-11}$ J/m ($d \approx 3.86$ nm for $\mu_0 M_s = 1.48$ T) [31].

jump in the transverse magnetization component increases. Studying the corresponding domain images (see Fig. 8), a superdomain structure appears around H_{BN} which expands progressively from the stripe center towards its edges as the transversal field amplitude is increased.

High resolution imaging of the domain walls (not shown due to weak contrast) revealed that the surface intensity of the former dark domain walls changed to be bright within the area of the brighter superdomains. Consequently, the magnetization jump observed in the local domain magnetization curves under the influence of a transversal magnetic field goes along with the expected transformation of the domain walls from asymmetric Bloch walls to asymmetric Néel walls. This conclusion is supported by the quantitative agreement between the experimental magnetization change and the theoretically predicted magnetization change from the asymmetric Bloch to the asymmetric Néel wall branch (compare thin solid lines in Fig. 7). Upon decreasing the field amplitude the process is reversed (not shown): At a critical field $|H_{NB}| < |H_{BN}|$ darker superdomains appear close to both stripe edges and expand towards the stripe center as H is further decreased. Consequently, H_{BN} corresponds to the reconversion of asymmetric Néel to asymmetric Bloch walls. The jump of the domain magnetization constitutes an additional contribution to the transversal magnetization component due to the interaction of neighboring Néel wall tails. In order to quantify the strength of the interaction between adjacent asymmetric Néel walls for different film thicknesses and domain wall spacings w, the magnetization change Δm ($\Delta m_x(w/2)$ in the notation of Sec. II) was deduced from the corresponding domain magnetization curves as sketched in the inset in Fig. 7. By linearly extrapolating the Néel wall branch of the minor magnetization curves to $H = 0$, the magnetization change due to the wall transition $\Delta m = \frac{M(H=0)}{M_s}$ is quantified independently of the transition fields H_{BN} and H_{NB}, similar to the applied procedure resulting in Fig. 4. Thereby Δm can be compared to the values derived by the presented model where the wall transition fields are not known. Figure 9 compares the experimental and theoretical values of Δm obtained for stripes with a thickness of 102 nm, 153 nm, and 212 nm.

As already obvious from Fig. 7 the interaction strength between neighboring Néel wall segments qualitatively increases as the domain wall spacing is reduced, which results in an increase of Δm. For a film thickness of 102 nm and 153 nm, the experimental values scatter around the theoretical values calculated by using the reduced model (see Sec. II). Hence, quantitative agreement between model and experiment is observed for a film thickness of 102 nm and 153 nm. Whereas the model predicts a slight decrease of the interaction strength between neighboring Néel wall tails (reduction in Δm) when increasing the film thickness to 212 nm, the experimental values do not follow this trend. On one hand, this may mean that the reduced model is not suited for the description of domain walls in CoFeB films that exceed a critical thickness. The fact that the samples in Table I do not clearly satisfy the regime $Q(t/d)^2 \ll 1$ might indicate that the breakdown of the reduced model occurs within the range

$$\begin{aligned} 1.5 &\approx 0.93 \times 10^{-3} \cdot (153/3.86)^2 \\ &\lessapprox Q(t/d)^2 \\ &\lessapprox 1.16 \times 10^{-3} \cdot (212/3.86)^2 \approx 3.5. \end{aligned}$$

On the other hand, this deviation could be due to slightly varying material parameters for the different depositions, in particular the exchange constant and saturation magnetization. It has been observed that the theoretical predictions of Δm are very sensitive to slight changes of the material parameters.

IV. CONCLUSION

Both for a single wall in an extended ferromagnetic film as well as a system of interacting domain walls, we have reviewed mathematically rigorous reduced models that describe and quantify the splitting of asymmetric domain walls into a stray-field free core and extended logarithmic tails. In addition, the reduced model for interacting walls predicts the average hard-axis magnetization within the domains.

In order to verify the prediction (3), hard-axis magnetization loops for the hysteretic transition between asymmetric Bloch and interacting asymmetric Néel walls have been measured in $Co_{40}Fe_{40}B_{20}$ films of thicknesses 102 nm, 153 nm, and 212 nm. While the instability fields for the transition from asymmetric Bloch to Néel wall and vice versa seem inaccessible within the reduced model, it reliably predicts the magnetization curves for asymmetric Bloch and Néel walls in the two thinner samples. In the film of thickness 212 nm, the reduced model underestimates the measured data by a factor of 2, which may indicate that the validity limit of the reduced models can be found within the range $1.5 \lessapprox Q(t/d)^2 \lessapprox 3.5$.

By evaluating Eq. (5) for various field strengths and anisotropies $Q \in \{2.5 \times 10^{-4}, 1.5 \times 10^{-3}\}$ (corresponding to CoFeB and permalloy) and determining the energetically favored domain wall among symmetric (characterized by $\theta = 0$) and asymmetric ($\theta > 0$) Néel and asymmetric Bloch walls, we have obtained phase diagrams that qualitatively agree with the previously available results (see Ref. [1], Fig. 3.80). Since the latter are based on numerical simulations, some of them not properly including the effect of extended tails of asymmetric Néel walls, we propose using the reduced models (4) and (5) as an easy-to-use and potentially more precise means of determining the energy and internal structure of domain walls in ferromagnetic films of medium thickness. In particular, we propose using Eq. (5) as wall energy density in domain theory. In this way, employing the well-known ansatz for the cross-tie configuration, an estimate for the energy of this domain wall microstructure can presumably also be obtained. Furthermore, by presenting an alternative derivation of the periodic reduced model (4), we demonstrate the equivalence of the energy- [20,21] and torque-balance-based approaches to studying the structure of asymmetric domain walls. Possible and desirable extensions consist of a verification of the reduced models and their estimated range of validity in a larger class of samples and ferromagnetic materials, as well as deriving predictions for the instability fields marking the transition between the two asymmetric wall types.

ACKNOWLEDGMENT

L.D. acknowledges support of the Max Planck Institute for Mathematics in the Sciences, Leipzig.

[1] A. Hubert and R. Schäfer, *Magnetic Domains - The Analysis of Magnetic Microstructures*, 1st ed. (Springer, Berlin, Heidelberg, New York, 1998), pp. xxvii and 686.
[2] E. Huber Jr, D. Smith, and J. Goodenough, J. Appl. Phys. **29**, 294 (1958).
[3] F. Alouges, T. Rivière, and S. Serfaty, ESAIM Control Optim. Calc. Var. **8**, 31 (2002), a tribute to J. L. Lions.
[4] M. J. Donahue, Adv. Condens. Matter Phys. **2012**, 908692 (2012).
[5] B. N. Filippov, M. N. Dubovik, and V. V. Zverev, J. Magn. Magn. Mater. **374**, 600 (2015).
[6] A. Hubert, Phys. Status Solidi B **32**, 519 (1969).
[7] A. Hubert, Phys. Status Solidi B **38**, 699 (1970).
[8] K. Rivkin, K. Romanov, Y. Adamov, A. Abanov, V. Pokrovsky, and W. Saslow, Europhys. Lett. **85**, 57006 (2009).
[9] C. Hengst, M. Wolf, R. Schäfer, L. Schultz, and J. McCord, Phys. Rev. B **89**, 214412 (2014).
[10] A. Hubert, Czech. J. Phys. B **21**, 532 (1971).
[11] R. Kirchner and W. Döring, J. Appl. Phys. **39**, 855 (1968).
[12] H. Riedel and A. Seeger, Phys. Status Solidi B **46**, 377 (1971).
[13] C. Melcher, Arch. Ration. Mech. Anal. **168**, 83 (2003).
[14] R. Ignat and F. Otto, J. Eur. Math. Soc. (JEMS) **10**, 909 (2008).
[15] M. Chermisi and C. B. Muratov, Nonlinearity **26**, 2935 (2013).
[16] A. LaBonte, J. Appl. Phys. **40**, 2450 (1969).
[17] D. V. Berkov, K. Ramstöck, and A. Hubert, Phys. Status Solidi A **137**, 207 (1993).
[18] S. W. Yuan and H. N. Bertram, Phys. Rev. B **44**, 12395 (1991).
[19] B. N. Filippov, L. G. Korzunin, and F. A. Kassan-Ogly, Phys. Rev. B **64**, 104412 (2001).
[20] L. Döring, R. Ignat, and F. Otto, JEMS **16**, 1377 (2014).
[21] L. Döring, Asymmetric domain walls in soft ferromagnetic films, Dissertation, Universität Leipzig, 2015.
[22] A. DeSimone, R. V. Kohn, S. Müller, and F. Otto, in *The Science of Hysteresis*, Vol. 2, edited by G. Bertotti and I. Mayergoyz (Elsevier Academic Press, Kidlington, UK, 2005), Chap. 4, pp. 269–381.
[23] F. Otto, in *Proceedings of the International Congress of Mathematicians, Vol. III (Beijing, 2002)* (Higher Ed. Press, Beijing, 2002), pp. 829–838.
[24] Indeed, $\cos\alpha_{\rm opt} \notin \{\cos\theta, H\}$ can be ensured if $\frac{w}{t}\ln\frac{w}{t} \sim \frac{1}{Q}$. Solving for $\frac{w}{t}$ as a function of Q in the regime $Q \ll 1$, one finds $\frac{w}{t} \sim 1/(Q\ln\frac{1}{Q})$.
[25] Due to the limited width of stray-field free walls, $E_{\rm core}(\theta)$ is accessible to brute-force numerical simulation: First note that due to the scaling invariance of $\int |\operatorname{grad}\vec{m}|^2 dA$ in two spatial dimensions, it suffices to determine $E_{\rm core}(\theta)$ for films of nondimensional thickness 1. Then, a finite-difference approximation of the Euler-Lagrange equation for $E_{\rm core}(\theta)$ is solved with the help of a relaxed Newton method (and PARDISO [32] as linear solver), using initial data that resemble asymmetric Néel and Bloch walls. We remark that in contrast to previous studies [17], we find that the energy of asymmetric Bloch walls does *increase* with increasing external field. This difference we attribute to a finer resolution of the vortex in the domain wall core. For small domain wall angles $\theta \approx 0$, a rigorous asymptotic expansion of the wall energy $E_{\rm core}(\theta) \approx 4\pi\sin^2\theta + \frac{148}{35}\pi\sin^4\theta$ (relative error to numerics for stray-field free Néel walls $<15\%$) and the minimizer is also available. The latter confirms the nonmonotonic rotation of asymmetric Néel walls on the film

surface, leading to the experimentally visible double contrast in the wall core. Details can be found in Ref. [33].

[26] With a refined ansatz for the bulk energy of the wall tails, the scaling of their width $w_{\text{tails}} \sim t/Q$ can actually be derived by this approach.

[27] In the single-wall case, one can also read off that the solution $m_{\text{out},x}$ must vary on the scale t/Q, which is the relevant length scale for this equation.

[28] To leading order in $Q \ll 1$, the constraint of vanishing stray field creates a topological barrier between the asymmetric wall cores [33–35]. This excludes a continuous transition between the two wall types. Identifying the corresponding instability fields therefore seems to require analyzing the wall energy or the torque-balance equation at higher orders in $Q \ll 1$.

[29] Samples were prepared by K. Kirsch at the IPHT Jena with a Cyberite sputtering tool.

[30] A. Hubert, J. Magn. Magn. Mater. **35**, 249 (1983).

[31] A. Conca, J. Greser, T. Sebastian, S. Klingler, B. Obry, B. Leven, and B. Hillebrands, J. Appl. Phys. **113** 213909 (2013).

[32] O. Schenk and K. Gärtner, Future Generation Computer Systems **20**, 475 (2004).

[33] L. Döring and R. Ignat, Arch. Rat. Mech. Anal. (2015), doi:10.1007/s00205-015-0944-0.

[34] A. Hubert, *Theorie der Domänenwände in geordneten Medien* (Springer-Verlag, Berlin, 1974).

[35] M. Labrune, S. Hamzaoui, I. Puchalska, and A. Hubert, J. Magn. Magn. Mater. **58**, 227 (1986).